

# High-resolution total-internal-reflection fluorescence microscopy using periodically nanostructured glass slides

Anne Sentenac, Kamal Belkebir, Hugues Giovannini, and Patrick C. Chaumet\*

Institut Fresnel (UMR 6133), CNRS, Aix-Marseille Université, Campus de Saint Jérôme, 13013 Marseille, France

\*Corresponding author: patrick.chaumet@fresnel.fr

Received April 16, 2009; revised September 9, 2009; accepted October 9, 2009;  
 posted October 13, 2009 (Doc. ID 109934); published November 9, 2009

We compare the performance of a total-internal-reflection fluorescence microscope under varying illumination and substrate conditions. The samples are deposited on a standard homogeneous glass slide or on a grating and illuminated by one or two interfering beams at various incident angles. A conjugate gradient with positivity *a priori* information is used to reconstruct the fluorophore density from the images. Numerical studies demonstrate that when the sample lies on an optimized grating, the lateral resolution of the microscope is greatly improved, up to fourfold, the best result being obtained when the grating is illuminated by two interfering beams. © 2009 Optical Society of America

OCIS codes: 110.0180, 180.2520, 180.3170, 050.2770.

## 1. INTRODUCTION

Optical fluorescence microscopy (OFM) is a widely used imaging tool in biology to study tissues at the scale of cells down to single molecules [1–3]. Unfortunately, the resolution of this far-field imaging technique is fundamentally limited by the diffraction process. Point scanning confocal microscopes obtain at best a lateral resolution (perpendicular to the optical axis) of  $\lambda/3$ , where  $\lambda$  is the illumination wavelength, i.e., several hundreds of nanometers [4]. Hence, improving the spatial resolution of far-field fluorescence microscopes below 100 nm has become a major challenge in the last ten years and has spurred the emergence of many innovative techniques [5].

Structured illumination microscopy has shown its potential for ameliorating the resolution in both the lateral (perpendicular to the optical axis) and the axial (along the optical axis) directions while keeping a wide-field configuration [6]. In this approach, the sample is illuminated by a periodic light grid stemming from the interference of two or three coherent beams (standing-wave pattern). Images of the sample are recorded for different positions of the grid, and the fluorescence density is retrieved numerically using an inversion algorithm [7,8]. The smaller the period of the light grid, the better the resolution. This technique has been extended to total-internal-reflection fluorescence microscopy (TIRFM), in which the excitation field is an evanescent wave obtained through the total internal reflection of the beam at a glass/air interface [9,10]. This configuration is well adapted to surface imaging inasmuch as only the fluorescent markers close to the interface are strongly illuminated. TIRFM is widely used in biological studies, especially for the observation of cell plasma membranes or biomolecular dynamics [11]. The higher resolution of the standing-wave TIRFM (SW-TIRFM) stems from the fact that the excitation light grid

has a period of  $(\lambda/2n_s)\sin\theta$ , where  $n_s$  is the refractive index of the high-index material whence the illumination comes and  $\theta$  is the angle of incidence. Fundamentally, the lateral and axial resolution of SW-TIRFM is monitored by the available high refractive index of the substrate, typically 1.45 for a convenient prismless, objective-launched TIRFM. Recently, this method has been shown to achieve a lateral resolution of approximately 100 nm [10] for an illumination wavelength of 500 nm while keeping the 100 nm axial resolution of conventional TIRFM.

To further improve the resolution, it is possible to take advantage of the saturation process that monitors the fluorescence at high power. The saturated structured illumination microscope [12,13] has been shown to exhibit a resolution of the order of a few tens of nanometers. Yet, this nonlinear phenomenon requires high-power pulsed lasers with an increased risk of photobleaching and photodisruption in comparison with conventional fluorescence imaging [6,12]. More recently, it has been proposed to ameliorate the resolution by reducing the period of the structured illumination below that of the standing-wave pattern, i. e., below the diffraction limit. This can be done by replacing the conventional glass slide of the microscope by a periodically nanostructured glass slide, (hereafter called grating) [14]. The grating is designed so as to generate a movable highly contrasted light grid with a period smaller than half the excitation wavelength. The interest of this approach is that it relies only on linear processes and thus can be implemented with low-power lasers and with any fluorescent markers.

In this work, we present an extended numerical study of grating-assisted TIRFM. We compare the resolution of TIRFM using homogeneous illumination, standing-wave illumination, homogeneous illumination on a grating substrate, and standing-wave illumination on a grating sub-

strate. We describe the optimization process of the grating and present an efficient inversion algorithm for retrieving the fluorophore distribution.

## 2. SIMULATION OF A TIRFM EXPERIMENT

We consider a sample made of one layer of fluorescent beads of diameter 20 nm deposited on a substrate, either a standard glass slide or a grating. The sample is placed at the focal object plane of an immersed objective with numerical aperture  $NA=1.45$ ; see Fig. 1. The intensity that is recorded at the image plane of the microscope can be simulated by

$$I_l^{\text{mes}}(\mathbf{r}) = [(O \times E_l) \otimes P](\mathbf{r}) + B(\mathbf{r}), \quad \text{for } l = 1, \dots, N, \quad (1)$$

where  $O(\mathbf{r})$  is the fluorophore density,  $P(\mathbf{r})$  is the point spread function of the microscope,  $I_l^{\text{mes}}(\mathbf{r})$  is the  $l$ th recorded intensity on the image plane of the microscope,  $E_l(\mathbf{r})$  is the excitation light above the substrate for the  $l$ th illuminations, and  $B(\mathbf{r})$  represents the noise of the system. In the following, we consider that the incident power and the time of exposure of the camera are chosen in such a way that one bead radiates 1000 photons on average. The noise  $B(\mathbf{r})$  is taken equal to a Gaussian random variable with a varying variance  $[(O \times E_l) \otimes P](\mathbf{r})$  plus a Gaussian random variable with a fixed variance equal to 1% of the maximum of  $[(O \times E_l) \otimes P](\mathbf{r})$ . With these formulas, we simulate approximately the Poisson noise due to the fluorescence phenomenon and a background noise. In

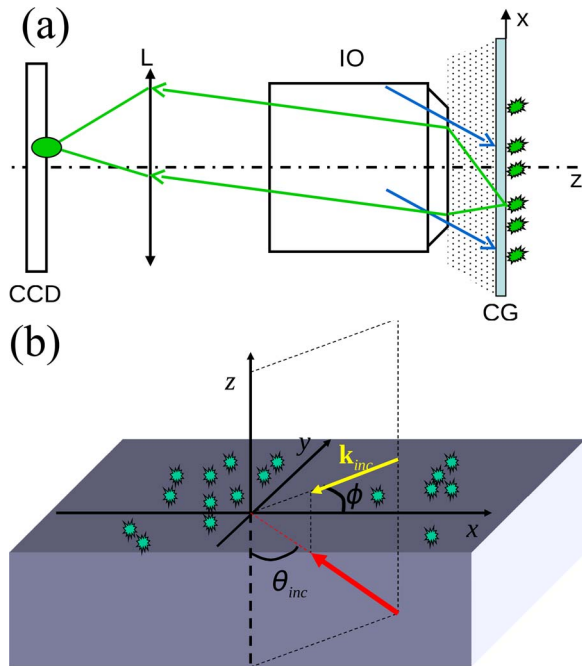


Fig. 1. (Color online) Schematic view of the TIRFM that is simulated in this work. (a) The fluorophores deposited on the substrate (glass slide: CG) are illuminated by a parallel beam that is totally reflected at the glass/air interface. IO is an inversion objective, and the image of each fluorophore is formed on the CCD camera, through the optical system (IO, L). (b)  $\theta_{\text{inc}}$  is the incident polar angle and  $\phi$  is the azimuthal angle.  $\mathbf{k}_{\text{inc}}$  is the tangential component of the incident wave vector.

our simulations, we consider only very thin samples, and we restrict our investigation to the two-dimensional images obtained at the focal plane of the microscope. The point spread function is given by the Airy function,

$$P(r) = \left( \frac{J_1(k_0 NA r)}{r} \right)^2, \quad (2)$$

where  $r = \sqrt{x^2 + y^2}$ ,  $k_0 = 2\pi/\lambda$  is the emitted wavenumber,  $\lambda = 650$  nm, and  $NA = 1.45$  is the numerical aperture of the objective. It is assumed in Eq. (1) that the point spread function is homogeneous, i.e., that it does not vary with respect to the position on the substrate plane. This assumption can be questioned when the substrate is a periodically nanostructured glass slide. Thanks to the reciprocity theorem, we have checked that the power emitted by a fluorophore within the collection solid angle of the objective did not vary more than 15% when the fluorophore was moved over the grating. In all examples, we use  $N = 12$  illuminations, and we reconstruct the fluorophores density  $O$  with the same inversion algorithm.

## 3. DESCRIPTION OF THE ILLUMINATION CONFIGURATIONS

We consider four different illumination configurations, depicted in Fig. 2. In the first one, Fig. 2(a), the sample is deposited on a homogeneous glass slide and is illuminated from below by one plane wave with polar angle  $\theta_{\text{inc}} = 65$  deg and 12 different azimuthal angles  $\phi = n\pi/6$ ,  $n = (0, \dots, 11)$ . The polar angle is chosen beyond the critical angle at the glass/air interface so that the light intensity decays exponentially as one moves away from the glass slide. Whatever the azimuthal angle, one obtains a uniform excitation light on the substrate. We record 12 images to be consistent with the other measurements and, in particular, to have the same sensitivity to noise.

In the second case, the sample is illuminated by two interfering plane waves that create a standing-wave pattern [10,16] [see Fig. 2(b)]. The polar incident angles of

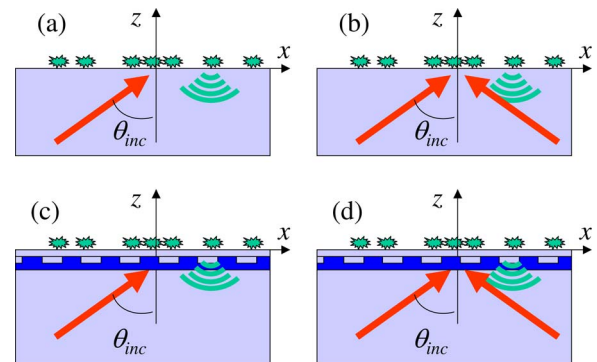


Fig. 2. (Color online) Illumination configurations. (a) Glass slide illuminated homogeneously by a plane wave under total internal reflection. (b) Glass slide illuminated by a standing-wave pattern. The periodic intensity pattern above the substrate is generated by the interference of two plane waves. (c) Grating illuminated by one plane wave. The period of the intensity pattern just above the grating can be much smaller than that obtained in (b). (d) Grating illuminated by two interfering plane waves. The intensity pattern above the grating is not periodic in general.

the two beams are  $\theta_{\text{inc}} = \pm 65$  deg, and we take four different azimuthal angles  $\phi = n\pi/4$ ,  $n = (0, 1, 2, 3)$ . For each incidence, the relative phase  $\psi$  between the two beams is varied three times  $\psi = n2\pi/3$ ,  $n = (0, 1, 2)$  so that eventually 12 images are recorded. Basically, the excitation light at  $z=0$ , just above the substrate, can be modeled by

$$E_i(\mathbf{r}) = A|\exp(i\mathbf{k}_{\text{inc}} \cdot \mathbf{r}) + \exp(-i\mathbf{k}_{\text{inc}} \cdot \mathbf{r} + i\psi)|^2, \quad (3)$$

where  $\mathbf{k}_{\text{inc}} = n_s(2\pi/\lambda')\sin\theta_{\text{inc}}\hat{\mathbf{u}}$ , with  $\hat{\mathbf{u}} = \cos\phi\hat{\mathbf{x}} + \sin\phi\hat{\mathbf{y}}$ ,  $\mathbf{r} = (x, y)$ ,  $\lambda' = 630$  nm is the excitation wavelength, and  $n_s = 1.5$  is the refractive index of the substrate. The standing-wave pattern is depicted in Figs. 3(a) and 3(b) for  $\psi=0$  and  $\psi=2\pi/3$ , respectively.

In the third configuration, the sample is deposited on an optimized grating and is illuminated by one plane wave with electric field parallel to the substrate (TE polarization), polar angle  $\theta_{\text{inc}} = 65$  deg, and 12 different azimuthal angles  $\phi = n\pi/6$ ,  $n = (0, \dots, 11)$  [see Fig. 2(c)]. The electric field above a grating illuminated by a plane wave is pseudoperiodic with the same periodicity as the grating. The light intensity at  $z=0$  just above the grating can be modeled by the square of a Rayleigh series [17],

$$E_i(\mathbf{r}) = \left| \exp(i\mathbf{k}_{\text{inc}} \cdot \mathbf{r}) \sum_{n,m \in \mathbb{Z}^2} A_{n,m} \exp(i\mathbf{K}_{n,m} \cdot \mathbf{r}) \right|^2, \quad (4)$$

where  $\mathbf{K}_{n,m}$  is a vector of the reciprocal space of the grating. In our work, we consider a regular hexagonal grating with period  $d$ , so that  $\mathbf{K}_{n,m} = n\mathbf{K}_a + m\mathbf{K}_b$  with  $\mathbf{K}_a = \frac{2}{3}2\pi/d\hat{\mathbf{y}}$  and  $\mathbf{K}_b = 2\pi/d(\hat{\mathbf{x}} - \hat{\mathbf{y}}/\sqrt{3})$ . Due to the hexagonal symmetry of the grating, the intensity obtained above the grating for any incident azimuthal angle  $\phi_0$  can be de-

duced from that obtained with the azimuthal angle  $\phi_0 - \pi/3$  through a rotation of  $\pi/3$  about the  $z$  axis. The grating is optimized so that when it is illuminated under TE polarization with  $\theta_{\text{inc}} = 65$  deg and  $\phi = \pi/2$ , only  $A_{0,0}$  and  $A_{-1,0}$  are dominant in the Rayleigh series Eq. (4). This property can be obtained by using a resonant grating [18,19]. The optimization process and the optogeometrical characteristics of the designed grating are detailed in Appendix A. If  $|A_{0,0}|$  and  $|A_{-1,0}|$  are of the same order, one gets an interference pattern similar to that of a standing-wave illumination with a period  $d\sqrt{3}/2$ . Figures 3(c) and 3(d) show the intensity above the grating obtained for  $\phi = \pi/2$  and  $\phi = 3\pi/2$ , respectively. One observes that the period of the light grid is roughly half that of the standing-wave pattern depicted in Figs. 3(a) and 3(b). Moreover, the light grid in Fig. 3(c) is similar to that in Fig. 3(d) with a shift close to half its period. This shift depends on the relative phase between the amplitudes  $A_{0,0}$  and  $A_{-1,0}$ , which can be optimized thanks to the resonance phenomenon. Note that this light-grid shift is most important to ensure a homogeneous illumination of sample. We have checked that the amplitude variation of the excitation light averaged over all 12 incident angles is smaller than 2, while that obtained for one specific illumination is about 7.

In the fourth configuration, Fig. 2(d), the sample is deposited on the same grating as previously and is illuminated by two interfering plane waves with polar angle  $\theta_{\text{inc}} = \pm 65$  deg, three different azimuthal angles  $\phi = \pi/2 + n\pi/3$ ,  $n = (0, 1, 2)$ , and four different relative phases  $\psi = n\pi/2$ ,  $n = (0, 1, 2, 3)$ . In this case, the intensity just above

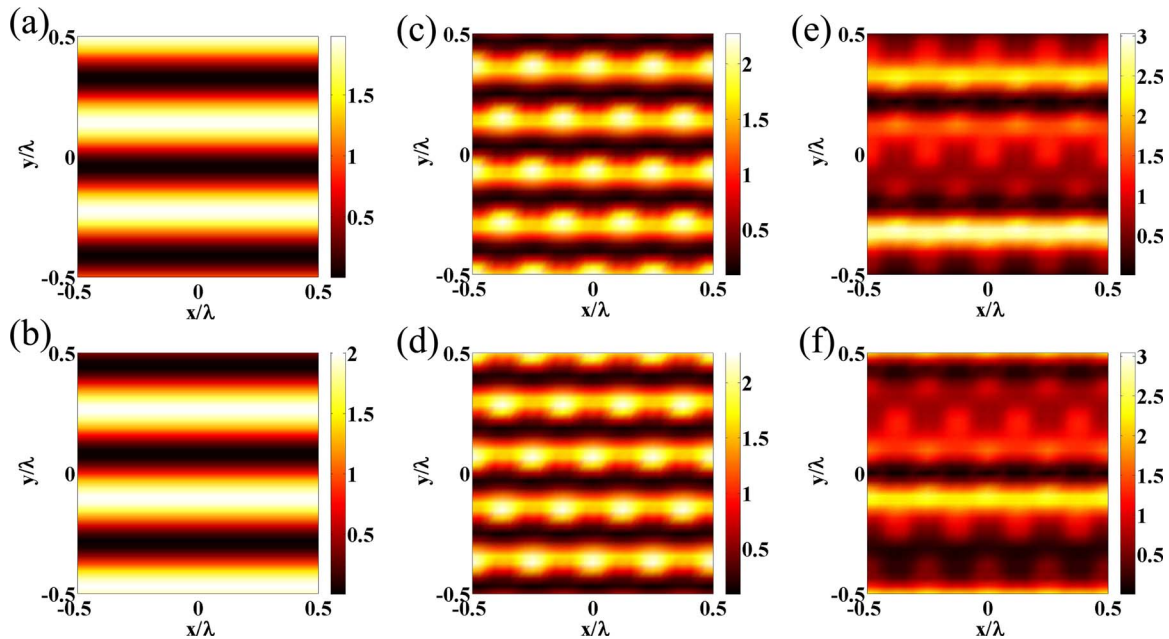


Fig. 3. (Color online) Excitation light patterns generated by the illumination configurations depicted in Fig. 2, (a), (b) Simulation of the field intensity just above the glass slide when the illumination is made of two interfering plane waves with  $\theta_{\text{inc}} = \pm 65$  deg and relative phase 0 and  $2\pi/3$  respectively. (c), (d) Simulation of the field intensity just above the grating when the illumination is an  $s$ -polarized plane wave with  $\theta_{\text{inc}} = 65$  deg and azimuthal angle  $\phi = \pi/2$  and  $\phi = 3\pi/2$ , respectively. The intensity is calculated with the rigorous Fourier modal method [17]. (e), (f) Same as (c), (d) but the grating is illuminated by two  $s$ -polarized plane waves with  $\theta_{\text{inc}} = \pm 65$  deg,  $\phi = \pi/2$ , same amplitude and relative phase 0 and  $\pi$ , respectively;

the grating is no longer periodic. Using the symmetry of properties of the structure, the intensity obtained for  $\theta_{\text{inc}} = \pm 65$  deg and  $\phi = \pi/2$  can be modeled by

$$E_l(\mathbf{r}) = \left| \exp(i\mathbf{k}_{\text{inc}} \cdot \mathbf{r}) \sum_{n,m \in \mathbb{Z}^2} A_{n,m} \exp(i\mathbf{K}_{n,m} \cdot \mathbf{r}) + \exp(-i\mathbf{k}_{\text{inc}} \cdot \mathbf{r} + i\psi) \sum_{n,m \in \mathbb{Z}^2} A_{n,m} \exp(-i\mathbf{K}_{n,m} \cdot \mathbf{r}) \right|^2. \quad (5)$$

Due to the choice of the polar and azimuthal angles,  $A_{0,0}$  and  $A_{-1,0}$  are dominant in the series appearing in Eq. (5). When the azimuthal angle is changed, the intensity pattern is simply rotated by  $\pi/3$  about the  $z$  axis. In Figs. 3(e) and 3(f), we plot the intensity existing just above the grating for two different relative phases,  $\psi=0$ , and  $\psi=\pi$  respectively. As previously, we checked that the amplitude variation of the intensity averaged over all 12 illuminations is about 2, while that for one specific illumination is about 7.

#### 4. DESCRIPTION OF THE INVERSION ALGORITHM

In standing-wave microscopy, the inversion algorithm that permits recovery of the density of fluorescence from the various images is usually based on a noniterative procedure, the first step of which consists of the calculation of the two-dimensional Fourier transform  $\tilde{I}_l^{\text{mes}}$  of the recorded intensities. It takes advantage of the phase variations of the Fourier transform of the illumination  $\tilde{E}_l$ , Eq. (3), obtained through the three translations of the standing-wave pattern, to retrieve, through a one-to-one correspondence, the Fourier amplitude of the density of fluorophores  $\tilde{O}$  on an extended Fourier domain [7,10,20]. Unfortunately, when the sample is deposited on a grating and illuminated by one plane wave, the different illumination patterns are obtained by changing the incident azimuthal angle, and there is no additional translation of the pattern as in standing-wave microscopy. Hence, it is impossible to use the same algorithm to infer  $\tilde{O}$  from  $\tilde{I}_l^{\text{mes}}$ . Thus, we derived a very general iterative inversion scheme to reconstruct the fluorophore density. We checked that this conjugate-gradient algorithm yielded the same result as the Fourier inversion procedure in the standard standing-wave configuration.

We first define a two-dimensional investigation domain  $\Omega$  at the surface of the glass slide (or of the grating), and we estimate the fluorophore density  $\hat{O}$  at the nodes of a regular meshing of  $\Omega$  so as to minimize the cost functional,

$$\mathcal{F}(\hat{O}) = \frac{\sum_{l=1}^L \|\tilde{I}_l^{\text{mes}} - \mathbf{A}(\hat{O}E_l)\|_{\Omega}^2}{\sum_{l=1}^L \|\tilde{I}_l^{\text{mes}}\|_{\Omega}^2} = W \sum_{l=1}^L \|\tilde{I}_l^{\text{mes}} - \mathbf{A}(\hat{O}E_l)\|_{\Omega}^2, \quad (6)$$

where  $\|\cdot\|_{\Omega}$  indicates the norm of the function on  $\Omega$ , and the calculated fluorescence intensity  $I_l$  for an estimation

of the density of fluorophores  $\hat{O}$  is cast in operator notation,

$$I_l = (\hat{O} \times E_l) \otimes P = \mathbf{A}(\hat{O}E_l). \quad (7)$$

We use a conjugate-gradient algorithm to solve this linear inverse problem [21].

The problem is now stated as finding the density of fluorophores such that the associated intensity, computed from Eq. (7), matches the measured one,  $I_l^{\text{mes}}$ . We propose in the present paper an iterative construction of  $\hat{O}$  using the following recursive relationship:

$$\hat{O}_n = \hat{O}_{n-1} + \alpha_n d_n, \quad (8)$$

where  $\hat{O}_n$  and  $\hat{O}_{n-1}$  represent estimations of the unknown density of fluorophores at iteration steps  $n$  and  $n-1$ , respectively. The correction  $\alpha_n d_n$  is composed of a scalar  $\alpha_n$  and an updating direction  $d_n$  taken equal to the well-known Polak-Ribière conjugate gradient direction [22,23],

$$d_n = g_n + \gamma_n d_{n-1}, \quad \text{with } \gamma_n = \frac{\langle g_n | g_n - g_{n-1} \rangle_{\Omega}}{\|g_{n-1}\|_{\Omega}^2}, \quad (9)$$

in which  $\langle \cdot | \cdot \rangle_{\Omega}$  is the inner product defined on  $\Omega$ . The function  $g_n$  is the gradient with respect to the density of fluorophores of the cost functional  $\mathcal{F}$ , Eq. (6). It is given by

$$g_n = -W \sum_{l=1}^L E_l \mathbf{A}^{\dagger} h_{l,n-1}, \quad (10)$$

with  $h_{l,n-1} = \tilde{I}_l^{\text{mes}} - \mathbf{A}(\hat{O}_{n-1}E_l)$  being the residual error in the model described by Eq. (7), while  $\mathbf{A}^{\dagger}$  is the adjoint operator of  $\mathbf{A}$ .

The scalar weight  $\alpha_n$  is determined at each iteration step  $n$  by minimizing the cost functional  $\mathcal{F}$  given by Eq. (6). Substituting the expression of  $\hat{O}_n$  given by Eq. (8) in the expression of  $\mathcal{F}$  given by Eq. (6) leads to a minimization of a polynomial with respect to  $\alpha_n$ . Hence,  $\alpha_n$  is determined analytically.

In many cases introducing the positivity *a priori* information of the parameter of interest, herein the density of fluorophores, improves the performance of the inverse scheme [22–24]. This is realized by retrieving an auxiliary function  $\hat{\xi}$  such that  $\hat{O} = \hat{\xi}^2$ . The inverse scheme presented above remains unchanged provided that the gradient  $g_n$  is replaced by the gradient  $g_{n;\hat{\xi}}$ , which is the gradient of the cost functional  $\mathcal{F}$  with respect to  $\hat{\xi}$  instead of  $\hat{O}$ :

$$g_{n;\hat{\xi}} = -2W \sum_{l=1}^L E_l \hat{\xi} \mathbf{A}^{\dagger} h_{l,n-1}. \quad (11)$$

Note that our inversion algorithm requires knowledge of the excitation pattern  $E_l$ . Small errors on  $E_l$  can cause artifacts or distorted images. Hence, it will be necessary, in practice, to accurately evaluate  $E_l$  prior the inversion, either with cross-correlation techniques such as those already implemented in standing-wave microscopy [8] or with an optimization process.

## 5. NUMERICAL RESULTS AND DISCUSSION

When the sample is illuminated by a homogeneous beam, the recorded intensity  $I$  is equal to the density of fluorophores  $O$  convoluted by the point spread function  $P$  of the microscope. The resolution of the image is given by the full width at half-maximum of  $P$  which, for  $NA=1.45$ , is about  $0.4\lambda$ . This assertion is illustrated in Figs. 4(a) and 4(b), which display a simulation of a TIRFM experiment. Figure 4(a) shows a theoretical sample made of randomly scattered beads, while Fig. 4(b) shows the image that would be recorded on a CCD camera if the sample were illuminated homogeneously.

An insight on the ideal resolution of a given imaging configuration can be obtained by estimating the domain of spatial frequencies of  $O$  that is theoretically accessible from  $I_l$ . The larger this domain, the better the resolution. This estimation is easily done when the illumination is homogeneous. It suffices to Fourier transform the recorded intensity  $I$ ,  $\tilde{I}=\tilde{O}\tilde{P}$ , where  $\tilde{I}$ ,  $\tilde{O}$ ,  $\tilde{P}$  are the Fourier transforms of  $I$ ,  $O$ , and  $P$ , respectively. In an ideal non-noisy system,  $\tilde{O}$  is accessible on the spectral domain  $S$  where  $\tilde{P}$  is nonnull. With the chosen point spread function,  $S$  is a disk of radius  $2NAk_0$ . This low-pass filter gives a resolution of about  $0.25\lambda$  for  $NA=1.45$ . There exist many deconvolution techniques that permit amelioration of the images when the point spread function is known [25]. In the present work, we used the iterative reconstruction algorithm presented in Section 4. Figures 4(c) and 4(d) display the density of fluorescence obtained by deconvoluting the CCD image, Fig. 4(b), without and with the positivity information, respectively. Hereafter, we will always use the positivity information in the reconstruction procedure.

In the standard standing-wave configuration, Fig. 2(b), the Fourier amplitude of the density of fluorophores  $\tilde{O}$  can be obtained on the extended Fourier domain  $S=\{\mathbf{k}, k$

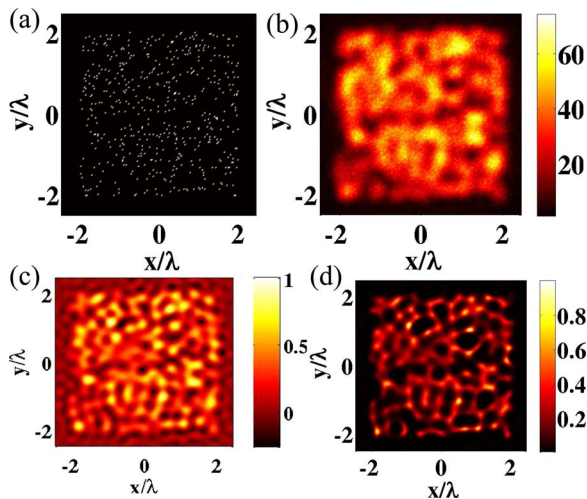


Fig. 4. (Color online) Simulation of a TIRFM experiment. (a) Theoretical sample: (beads with a diameter of 20 nm, randomly scattered on a glass slide). (b) Simulation of the image recorded on the CCD camera using a homogeneous illumination. (c) Deconvolution of (b) with the conjugate-gradient algorithm depicted in Section 4 without assuming the positivity of the density of fluorescence. (d) Same as (c) but the algorithm accounts for the positivity.

$<2NAk_0\} \cup \{\mathbf{k}, |\mathbf{k} \pm 2\mathbf{k}_{\text{inc}}| < 2NAk_0\}$  [7,20], where  $2k_{\text{inc}}$  represents the spatial frequency of the light grid illuminating the sample. The higher  $k_{\text{inc}}$ , the larger  $S$  and the better the resolution. With the chosen standing-wave pattern, the accessible spectral domain obtained with structured illumination is almost twice as large as that obtained with homogeneous illumination. Thus, one expects to ameliorate the resolution of the image by a factor of 2.

When the sample is deposited on a grating, one cannot easily infer  $\tilde{O}$  from  $\tilde{I}_l$  as in the standing-wave approach. However, we may still try to estimate the potential resolution of the imager from the analysis of the highest spatial frequencies of the light grid illuminating the sample. The intensity obtained above the grating when the latter is illuminated by one plane wave with  $\theta_{\text{inc}}=65$  deg and  $\phi_{\text{inc}}=\pi/2$  can be approximated by

$$E_l(\mathbf{r}) \approx |A_{0,0} + A_{-1,0} \exp(i\mathbf{K}_{-1,0} \cdot \mathbf{r})|^2. \quad (12)$$

This expression is close to that obtained with the standing-wave approach except that the spatial pulsation of the grid is now  $K_{-1,0}=4\pi/(d\sqrt{3})$  instead of  $2k_{\text{inc}}$ . With our periodically nanostructured substrate, the spatial pulsation of the grating light grid is found to be 1.7 greater than that of the standing-wave pattern.

When the grating is illuminated by two plane waves, the intensity above the substrate is no longer periodic. For  $\theta_{\text{inc}}=\pm 65$  deg and  $\phi=\pi/2$  and a phase difference of  $\psi$  between the two waves, it can be approximated by

$$E_l(\mathbf{r}) \approx |A_{0,0} \cos(\mathbf{k}_{\text{inc}} \cdot \mathbf{r} + \psi/2) + A_{-1,0} \cos[(\mathbf{k}_{\text{inc}} + \mathbf{K}_{-1,0}) \cdot \mathbf{r} + \psi/2]|^2. \quad (13)$$

In this case, the highest spatial frequency of the intensity pattern is  $2|\mathbf{k}_{\text{inc}} + \mathbf{K}_{-1,0}| \approx 1.3K_{-1,0}$ . Hence, illuminating the grating with two plane waves should ameliorate further the resolution of the image. It should be roughly four times better than that obtained with the homogeneous illumination and two times better than that obtained with the standing-wave pattern.

The successive amelioration of the resolution of the standard TIRFM with the standing-wave, the grating, and the standing-wave-grating configurations are illustrated in Fig. 5. The sample, made of beads with various interdistances, permits quantification of the resolution improvement brought about by the different configurations. The best resolution is obtained in the standing-wave-grating configuration, which permits one to distinguish two beads that are separated by  $\lambda/10$ . Note that when the grating is illuminated by only one plane wave, some beads are not properly retrieved due to the residual inhomogeneity of the average excitation. This problem disappears if the grating is illuminated by two interfering beams. To assess the ability of the different techniques to retrieve the fluorescence density of more complicated samples, we plot in Fig. 6 the reconstructed density of the random sample of beads depicted in Fig. 4 for the standing-wave, the grating, and the standing-wave-grating configurations. Once again, one observes that using the grating substrate improves the resolution substantially.

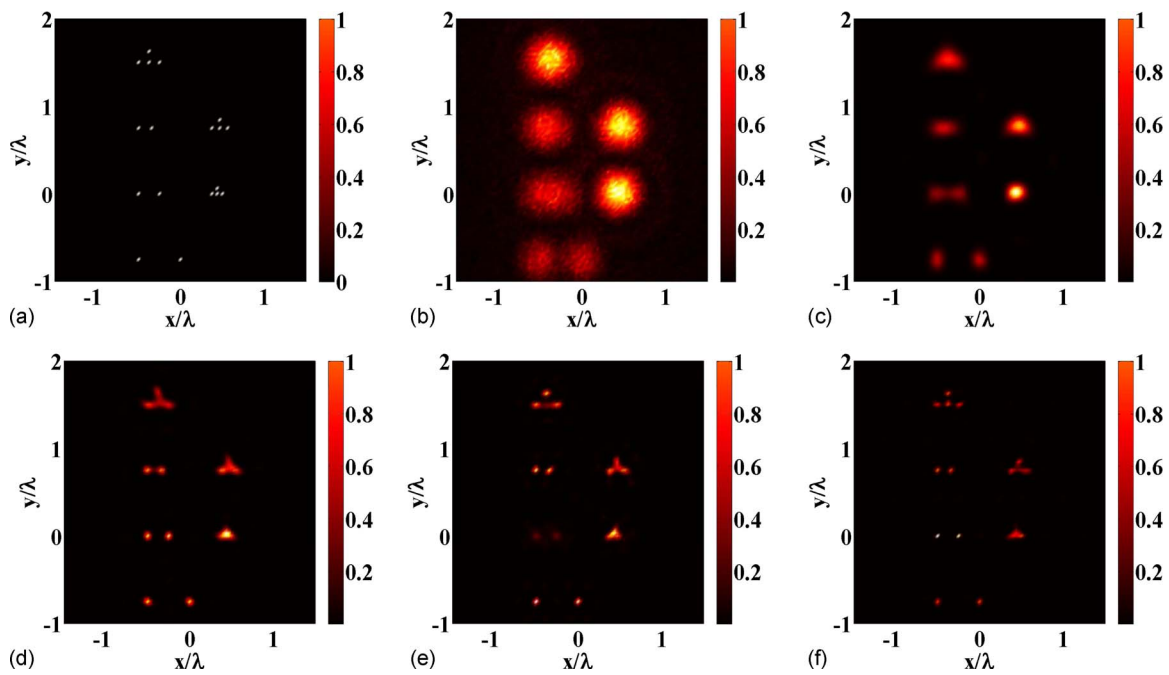


Fig. 5. (Color online) Illustration of the resolution improvement brought by the grating. (a) Theoretical sample: beads with a diameter of 20 nm that are separated by  $\lambda/2$ ,  $\lambda/4$ ,  $\lambda/6$ ,  $\lambda/8$  from bottom to top on the left side and  $\lambda/10$ ,  $\lambda/14$  from top to bottom on the right side. (b) Simulation of an image recorded on the CCD camera using homogeneous illumination. (c) Normalized density of fluorescence obtained with the iterative inversion procedure accounting for the positivity (Section 4) in the homogeneous configuration; see Fig. 2(a). (d) Same as (b) but in the standing-wave configuration; see Fig. 2(b). (e) Same as (b) but in the grating configuration; see Fig. 2(c). (f) Same as (b) but in the standing-wave grating configuration; see Fig. 2(d).

## 6. CONCLUSION

We analyze numerically the resolution improvement brought about by replacing the glass slide of a structured-illumination total-internal-reflection fluorescence microscope by an optimized grating. The grating is illuminated by one plane wave or by two interfering beams at various incident angles. It has been designed so that the periodic

intensity pattern obtained at its surface can be translated or rotated by changing the incident angle. Thus, the sample is homogeneously illuminated on average. We develop a versatile inversion algorithm based on a conjugate-gradient technique and accounting for the positivity of the unknowns to retrieve the fluorescence density of the sample from the images. The 160 nm period grating

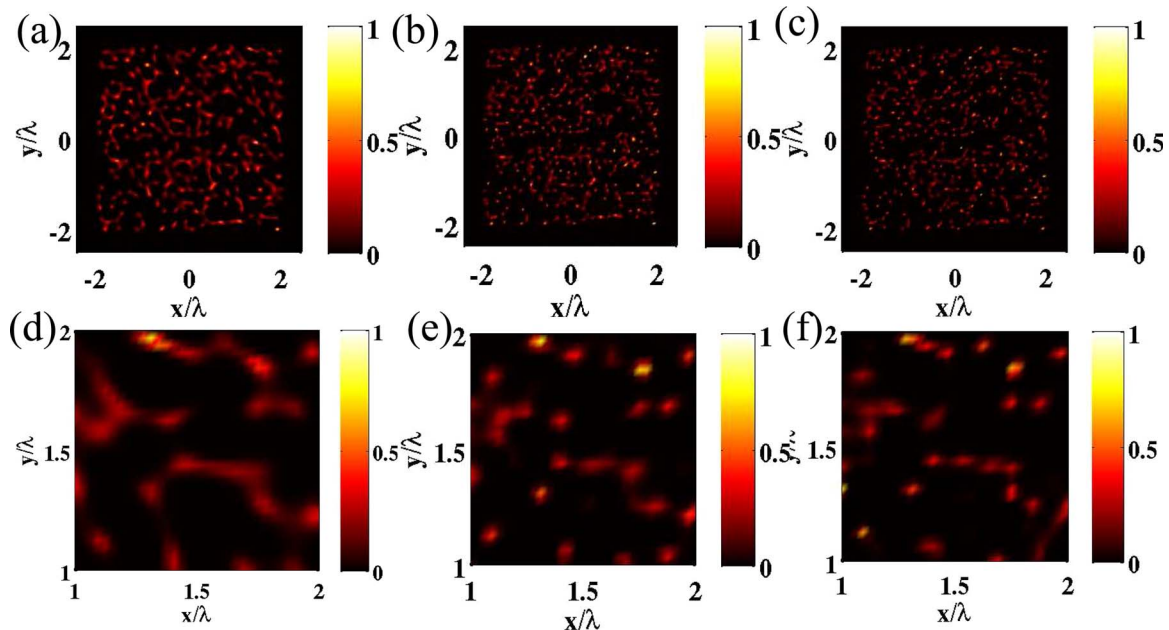


Fig. 6. (Color online) Reconstructed fluorescence density of the random sample depicted in Fig. 4. (a) Standing-wave configuration; see Fig. 2(b). (b) Grating configuration; see Fig. 2(c). (c) Standing-wave grating configuration; see Fig. 2(d). (d), (e), and (f) zoom of (a), (b), and (c) respectively.

optimized in this work permits one to obtain a resolution of about 60 nm, i.e., a fourfold improvement of resolution in comparison with conventional TIRFM. In theory, even better results could be obtained using gratings with smaller periods.

## APPENDIX A: OPTIMIZATION OF THE GRATING

The key issue of the approach presented in this work lies in the optimization of the grating substrate, which should exhibit two important properties. First, the intensity obtained above the grating for one incident angle should be highly contrasted, with high-spatial-frequency features. Second, the intensity averaged over all incident angles should be roughly homogeneous. This second property is essential to avoid the presence of blind spots on the sample. To obtain high-spatial-frequency features, it is convenient to design a grating with a period that is small compared with the wavelength (at least smaller than  $\lambda/3$  to expect a better resolution than a classical standing-wave illumination). Now, if the periodic permittivity modulation is weak (for example, an engraved glass slide), then, the zero-order amplitude  $A_{0,0}$  will be much larger than that of the higher-order terms. As a result, the intensity pattern above the grating will be poorly contrasted. Yet, if the permittivity contrast is high (for example, by placing periodically metallic particles on the glass slide), then changing the incident angles, polarization, or relative phases does not permit, in general, enough modification of the positions where the field is intense or weak, as they are linked to the jumps of permittivity. As a result, the average intensity exhibits blind spots where the fluorescence is never detected. To avoid these two pitfalls, we considered special kinds of gratings that are known as waveguide gratings or resonant gratings. The latter have been studied essentially for their filtering properties [18,19].

A resonant grating is basically a multilayer that is decorated by a periodic structuration. At the excitation wavelength  $\lambda'$ , the multilayer is designed to support a guided or surface mode, described by its wavenumber  $k_{\text{mode}}$ . If the incident angles and the period of the grating are chosen so that the phase-matching condition,

$$|\mathbf{k}_{\text{inc}} + \mathbf{K}_{-1,0}| \approx k_{\text{mode}}, \quad (14)$$

is satisfied, the incident wave couples to the mode through diffraction with the  $(-1,0)$  order. This resonance phenomenon specifically increases the  $(-1,0)$  amplitude in the Rayleigh series, Eq. (3). The main issue is then to design a multilayer supporting guided or surface modes with high wavenumbers in order to generate a light grid with the smallest period possible.

In previous work [14,26,27], we have considered very thin metallic films supporting high-spatial-frequency surface plasmons (the thinner the film, the higher the plasmon wavenumber). In this paper, following the recent study presented in [28], we have considered a dielectric multilayer supporting guided modes. Indeed, these structures appeared easier to fabricate. The wavenumber of guided modes depends essentially on the index of refraction of the guiding layer. Now, in optics, the refractive in-

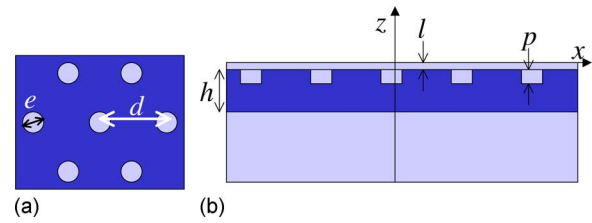


Fig. 7. (Color online) Schematic representation of the grating. (a) Top view. (b) Side view;  $d=157$  nm,  $e=50$  nm,  $h=88$  nm,  $l=19$  nm,  $p=50$  nm, incident wavelength  $\lambda=630$  nm.

dices of the lossless dielectrics that are generally used for waveguiding are smaller than 2.5, which limits  $k_{\text{mode}}$  to  $2.5k'_0$ , where  $k'_0=2\pi/\lambda'$ . Hence, to further increase the value of  $k_{\text{mode}}$ , we have considered a lossy semiconductor, silicon, which presents a high index of refraction with small losses  $n_{\text{Si}}=4.+i0.1$  at  $\lambda'=630$  nm. Of course, this material cannot be used for standard waveguiding applications since the mode propagates only over a few micrometers. Yet, it can be used for our application because the resonance phenomenon is strong enough to increase  $A_{-1,0}$  at the same level as  $A_{0,0}$  with an appropriate design of the periodic nanostructure. The resonant grating that is used in this work is made of one silicon layer of thickness  $h=88$  nm deposited on a glass substrate. This layer supports a TE guided mode with  $k_{\text{mode}} \approx 3.5k'_0$  at  $\lambda'=630$  nm. It is decorated by periodic holes on a triangular mesh. The period  $d$  is chosen so that Eq. (14) is satisfied for  $\theta_{\text{inc}}=65$  deg and  $\phi=\pi/2$ ,  $d=157$  nm. Note that to excite a TE guided mode in these conditions, the incident plane wave must be  $s$ -polarized; that is, the incident electric field is perpendicular to the plane of incidence. The diameter  $e=75$  nm and depth  $p=50$  nm of the holes are optimized to maximize the value of  $A_{-1,0}$ . To deal with a flat interface, the grating is planarized with a thin layer of resin that fills the holes  $n_{\text{resin}}=1.5$ . The geometry of the grating is depicted on Fig. 7.

## ACKNOWLEDGMENT

This research is supported by the Agence nationale de la recherche (ANR)-2008-Pnano-P052-36 Sonde Optique Ultra-Résolue pour l'Imagerie de Surface (SOURIS) project.

## REFERENCES

1. C. Zander, J. Enderlein, and R. A. Keller, eds., *Single Molecule Detection in Solution: Methods and Applications* (Wiley-VCH Verlag, 2003).
2. F. W. D. Rost, *Fluorescence Microscopy*, Vol. I (Cambridge Univ. Press, 1992).
3. F. W. D. Rost, *Fluorescence Microscopy*, Vol. II (Cambridge Univ. Press, 1995).
4. G. Cox and C. J. R. Sheppard, "Practical limits of resolution in confocal and non-linear microscopy," *Microsc. Res. Tech.* **63**, 18–22 (2004).
5. S. Hell, "Far-field optical nanoscopy," *Science* **25**, 1153–1158 (2007).
6. A. Stemmer, M. Beck, and R. Fiolka, "Widefield fluorescence microscopy with extended resolution," *Histochem. Cell Biol.* **130**, 807–617 (2008).
7. R. Heintzmann and C. Cremer, "Laterally modulated excitation microscopy: improvement of resolution by using a diffraction grating," *Proc. SPIE* **3568**, 185–196 (2007).

8. O. Mandula, "Patterned excitation microscopy," Master's thesis (Institute of Physics, King's College, 2008).
9. G. Cragg and P. So, "Standing wave total-internal reflection microscopy," *Opt. Lett.* **25**, 46–48 (2000).
10. E. Chung, D. Kim, and P. So, "Extended resolution wide-field optical imaging objective-launched standing-wave total internal reflection fluorescence microscopy," *Opt. Lett.* **31**, 945–947 (2006).
11. D. Toomre and D. J. Manstein, "Lighting up the cell surface with evanescent wave microscope," *Trends Cell Biol.* **11**, 298–303 (2001).
12. R. Heintzmann, T. M. Jovin, and C. Cremer, "Saturated patterned excitation microscopy: a concept for optical resolution improvement," *J. Opt. Soc. Am. A* **19**, 1599–1609 (2002).
13. M. Gustafsson, "Nonlinear structured-illumination microscopy: wide-field fluorescence imaging with theoretically unlimited resolution," *Proc. Natl. Acad. Sci. U.S.A.* **102**, 13081–13086 (2005).
14. A. Sentenac, K. Belkebir, H. Giovannini, and P. C. Chaumet, "Subdiffraction resolution in total internal reflection fluorescence microscopy with a grating substrate," *Opt. Lett.* **33**, 255–257 (2008).
15. A. L. Fehrembach, S. Enoch, and A. Sentenac, "Highly directive source devices using slab photonic crystal," *Appl. Phys. Lett.* **79**, 4280–4282 (2001).
16. R. Fiolka, M. Beck, and A. Stemmer, "Structured illumination in total internal reflection fluorescence microscopy using a spatial light modulator," *Opt. Lett.* **33**, 1629–1631 (2008).
17. L. Li, "New formulation of the Fourier modal method for crossed surface-relief gratings," *J. Opt. Soc. Am. A* **14**, 2758–2767 (1997).
18. D. Maystre, *Diffraction Gratings*, SPIE Milestones Series (SPIE Press, 1993).
19. A. L. Fehrembach, D. Maystre, and A. Sentenac, "Phenomenological theory of filtering by resonant dielectric gratings," *J. Opt. Soc. Am. A* **19**, 1136–1142 (2002).
20. J. Frohn, H. Knapp, and A. Stemmer, "True optical resolution, beyond the Rayleigh limit, achieved by standing wave illumination," *Proc. Natl. Acad. Sci. U.S.A.* **97**, 7232–7236 (2000).
21. P. C. Chaumet, K. Belkebir, and A. Sentenac, "Three-dimensional sub-wavelength optical imaging using the coupled dipole method," *Phys. Rev. B* **69**, 245405–7 (2004).
22. K. Belkebir and A. Sentenac, "High-resolution optical diffraction microscopy," *J. Opt. Soc. Am. A* **20**, 1223–1229 (2003).
23. K. Belkebir and A. G. Tijhuis, "Modified<sup>2</sup> gradient method and modified Born method for solving a two-dimensional inverse scattering problem," *Inverse Probl.* **17**, 1671–1688 (2001).
24. A. Dubois, K. Belkebir, and M. Saillard, "Retrieval of inhomogeneous targets from experimental frequency diversity data," *Inverse Probl.* **21**, S65–S79 (2005).
25. G. R. Ayers and J. C. Dainty, "Iterative blind deconvolution method and its applications," *Opt. Lett.* **13**, 547–549 (1988).
26. A. Sentenac, P. C. Chaumet, and K. Belkebir, "Beyond the Rayleigh criterion: grating assisted far-field optical diffraction tomography," *Phys. Rev. Lett.* **97**, 243901–4 (2006).
27. P. C. Chaumet, K. Belkebir, and A. Sentenac, "Numerical study of grating-assisted optical diffraction tomography," *Phys. Rev. A* **76**, 013814–7 (2007).
28. A. Sentenac and P. C. Chaumet, "Sub-diffraction light focusing on a grating substrate," *Phys. Rev. Lett.* **101**, 013901–4 (2008).